Title
MRI Probe for Cell-Targeted Imaging: Click-Functionalized Perfluorocarbon Nanoemulsions

Author
Perez, Adam Soufiane

Publication Date
2021

Peer reviewed|Thesis/dissertation

MRI Probe for Cell-Targeted Imaging: Click-Functionalized Perfluorocarbon Nanoemulsions

By

ADAM S. PEREZ
THESIS

Submitted in partial satisfaction of the requirements for the degree of

MASTER OF SCIENCE

in

Chemistry

in the

OFFICE OF GRADUATE STUDIES

of the

UNIVERSITY OF CALIFORNIA

DAVIS

Approved:

Angelique Louie, Chair

Eric Ahrens

Annaliese Franz

Committee in Charge

2021

Table of contents

Acknowledgments

I would like to gratefully acknowledge the generosity and trust of Eric Ahrens for allowing me to work in his lab at UCSD and learn from his highly talented team. I would like to thank Hongyan Xu, Benjamin Leach, Stephen Adams, and Chao Wang for putting up with all of my questions and challenging me to learn new methods with curiosity and confidence that I certainly reflect in my everyday life. I would like to thank the team at UCD, Selene (Junhan) Zhou, Kimberly Trevino, and Tom (Chuqiao) Tu for guiding me through the beginnings of my graduate career and helping me to develop a sense of humility and respect for different ideas and our unique insights. I would like to give the biggest thanks to Angie (Angelique) Louie, who is complete support and advocation of my abilities has led to this great opportunity to collaborate with UCSD. Her heightened sense for my potential was my guiding light when I was unsure of my own potential.

I would also like to thank my family for nurturing and building me from the start. Thank you for believing in me and all of my lofty dreams.

Abstract

As the epidemic of cancer continues to grow, so have new treatment plans to incorporate the latest findings about tumors. We present the idea of a noninvasive method of examining cancer cell-profiles with ^{19}F magnetic resonance imaging (MRI) molecular probes, perfluorocarbon nanoemulsions (PFC), to selectively label cancer-relevant immune cells. PFC nanoemulsions have exemplified their utility in tracking biodistribution of immunotherapies in *ex vivo* labeling. Herein, we propose a method of labeling selected immune cells *in vivo* by increasing cell affinity for the PFC tracer by coupling receptor-specific ligands. To perform this conjugation, we will functionalize the nanoemulsion surface by incorporating the strain-promoted [3+2] azide-alkyne cycloaddition (SPAAC) reagent, dibenzocyclooctyne (DBCO), in the surfactant layer to click with azide-modified ligands. We have examined the ability for SPAAC to occur and optimized conditions for targeting the tumor-associated macrophage phenotype (TAM) M2 with the ligand sulfated dextran (SD).

Abreviations used in this thesis

NMR – Nuclear magnetic resonance

PFC – Perfluorocarbon

DBCO - Dibenzocyclooctyne

NE - Nanoemulsion

MRI – Magnetic resonance imaging

AF – Alexafour

SD – Sulfated dextran

SDA- Sulfated dextran axide

IVIS – In vivo imaging system

DLS – Dynamic light-scattering

TME – Tumor microenivornment

SM – Starting material

SRA – Scavenger A1 receptor

PFOB – Perflurooctyl bromide

IV – Intraveneous

ROI – Regions of interest

SPAAC – Strain-promoted [3+2] azide-alkyne cycloaddition

PFPE – Perfluoropolyether

NHS – N-hydoxysuccinimide

RARE - Rapid acquisition with relaxation enhancement

FBS – Fetal bovine serum

FOV – Field of view

IACUC - Institutional animal Care and use committee

EYP – Egg-yolk phospholipid

DMEM – Dulbeccos modified eagles medium

TAM – Tumor associated macrophage

IHC – Immunohistochemistry

BLI – Bioluminesence imaging

Chapter 1: Introduction

1.1 In the search of macrophages

One of the most concerning issues regarding cancer is its ability to outmaneuver our immune systems and manipulate resistance to therapies. This resistance appears to be facilitated under the conditions of the tumor microenvironment (TME) which is composed of immune cells which can constitute up to 50% of its cancerous mass as seen in breast cancer. An early idea was proposed that at the onset of cancer, the immune system responds to cancer by activating T cells and macrophages against this progression[1]. However, beyond this early stage, the TME changes as a result of the abnormal variant tissue harboring dying and growing cells which release local danger signals to recruit macrophages to repair the tumor tissue. This repurposing of macrophages, classified as tumor associated macrophages (TAMs), starts various mechanisms to begin vascularization and immunosuppression of the area which nourish, proliferate, and protect the abnormal tumor growth[2].

To further complicate matters, not all macrophages possess these tumorigenic properties. It is proposed that there are two phenotypically differentiated classifications for macrophages roles: M1 types for proinflammatory and M2 anti-inflammatory behavior. It was determined that the TAMs possess tumorigenic properties that overlap with M2

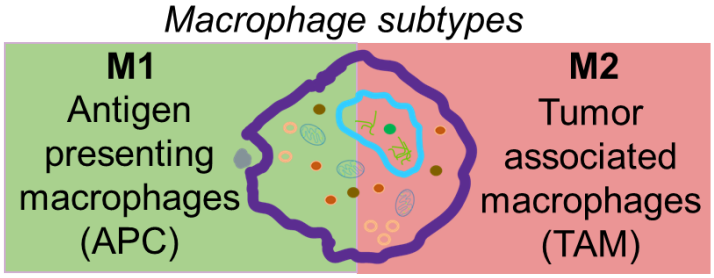

Figure 1.1. Macrophage subtypes

phenotype[3] (**Figure 1.1**). The pro-inflammatory macrophages are classified as M1 behavior by promoting cytotoxic environments while anti-inflammatory macrophages are classified as M2 behavior by stimulating cell growth. The M1/M2 dichotomy was understood as a degree of polarization between the two phenotypes based on the signals provided by the microenvironment[4]. In one study on ovarian cancer it was noted that that higher ratios of M1 to M2 type macrophages positively correlated with higher survival rates for patients[5]. Therefore, there is clinical value in distinguishing the degree of differentiation between these two sub-types reliably to provide practitioners diagnostic insight into the health of cancer patients.

In the search of identifying M1/M2 activity, various imaging methods for quantifying or identifying regions have been adapted. One such example was focused on using molecular detection probes to emit fluorescence in the near-infrared (NIR) region in the presence of nitrous oxide probe (NO), an M2-marker, to monitor the macrophagic changes from various drugs in real time[6]. Notably, most examples involving imaging M1/M2 macrophages use fluorescence based microscopy and visualize cells *ex vivo*, however *in situ* labeling would be more advantageous for screening patients for macrophages. Proposing solutions for imaging these important groups in of macrophages *in situ* would expand our imaging toolset with functionality for subsequent cell-type selectivity.

In the area of treatment research, there are efforts in polarizing the two groups from M1 to M2 type macrophages *in vivo*, and imaging the cells is one method to verify the efficacy of any proposed nanoemulsion for localization at a desired site for effect. One such method to control the nanoemulsion localization is receptor-based targeting.

Research in this area has been focused on delivery systems such as polymersomes, liposomes, carbon nanotube, dendrimers, and nanoemulsions which rely on conjugating the ligand to the particle to induce localization to the receptor of the targeted cell-type. The concept originated in the early advances in biology in the 1980s, properties of tumor cells were identified to overly express the transferrin receptor (TfR)[7], which proved to be a successful targeting-site when used for direct selective internalization of transferrin-toxin and transferrin-DNA conjugates into the tumor cell using liposomes[8]. As a result of successful examples of receptor-based targeting applications, we have greater support for implementation of this strategy.

1.2 Nanoemusions and ^{19}F MRI

In order to utilize the tumor's cellular profile for targeting purposes in treating cancers, patients are subjected to biopsies in the tumor region. While biopsies are the most common method for assessing a tumor's cellular profile, the method is invasive and often requires external imaging methods such as MRI or PET. Biopsies can cause potential damage to normal tissue surrounding the area, and usually requires 2 to 10 days of processing. [9,10].

As mentioned previously, imaging methods are often required with biopsies in order to locate tissue of interest. MRI is a safe and noninvasive method used to image tumors. Typically, measurements can be gathered using positive and negative contrast agents that are injected *in vivo.* Examples include gadolinium and superparamagnetic iron oxide (SPIO), which rely on intrinsic changes in T1 and T2 relaxation times to produce contrast within images. The major drawback to using contrast agents for imaging

purposes is that it is difficult to definitively determine regions of particle presence due to the different concentrations of protons surrounding the contrast agent.

In order to generate more distinguishable images in MRI, one promising method uses ^{19}F molecular probes which depends on dense concentrations of fluorine nuclei to produce hot-spot images within cells[11]. MRI experiments using perfluorocarbon nanoemulsions (PFC-NE) as molecular probes have shown its effectiveness in utilizing ^{19}F MRI measurements to overlay with ^{1}H MRI results to highlight fluorine-dense regions within their 3D environment[12]. Due to the lower biological abundance of the ^{19}F nuclei, regions have clear distinctions within images and their concentration is easily quantifiable with a standard or phantom present. PFC-NE have demonstrated their utility as MRI imaging probes for immune cell subtypes including visualizing dendritic cells (DC), natural killer cells (NK) and macrophages, and were able to reveal biodistribution and bioaccumulation upon *ex vivo* analysis[13]. However, straightforward in situ labelling presents a challenge of selective uptake by the desired cells.

Upon closer inspection of the chemical properties of the perfluorocarbon-types or PFCs used, their potential for cell labeling becomes more clear[14]. PFCs are considered molecules which typically have several C-F bonds. The energy barrier required to break the C-F is higher than most biological systems, rendering them mostly biologically inert[15]. Another feature is the ability for PFCs to display both lipo- and hydrophobic characteristics, which are well suited to resist dissolving in the cellular membrane[16]. The variety of PFC type used can also add dynamicity in imaging properties. Perfluoropolyether (PFPE) is a typical PFC used, and it is a long, linear polymer with many repeating units resulting in many chemically equivalent fluorine nuclei and

increases its overall sensitivity in ^{19}F MRI[17]. Perfluorooctyl bromide (PFOB) is another PFC-type which is smaller in length optimizing it to quicker clearance *in vivo* and possesses unique fluorine nuclei signatures.

Emulsification of the PFC is used to encase the PFC in stable droplets. Since the PFC itself is a dense oil being both highly hydrophobic and hydrophilic, it is stabilized in a colloidal suspension by surfactants which must be sonicated and homogenized by microfluidization to produce nanoemulsions of consistent sizes and charcteristics[18]. It has been shown that the surfactant layer can be altered to change its characteristics to enhance cellular uptake in specific cells[19], which has led to many methods for layer modification to be developed. Typically, surfactants for the preparation of PFC nanoemulsions (PFC-NE) are comprised of pluronics and phospholipids to generate small consistent droplets (~100-200 nm) and fluorine concentration can be easily measured in ^{19}F NMR prior to studies.

1.3 Functionalized nanoemulsions

A common strategy to achieve *in vivo* targeting of nanoemulsions is to adorn them with ligands with reported affinity for distinct cellular biomarkers. Reports typically have utilized a variety ligand types such as peptides, antibodies, polymers, and small molecules and. However, preparing nanoemulsions in for this purpose requires time and multistep procedures to generate ligand moieties along the emulsion surface. To streamline this process, we present a methodology to rapidly confer ligand-guided specificity with a simple and effective attachment using copper free click chemistry to attach ready-to-click nanoemulsions to the prospective ligands.

Strategies for functionalizing PFC nanoemulsions have been reported in two distinct preparations: pre-emulsification and post-emulsification. Pre-emulsification techniques rely on ligand conjugation before the high-pressure, microfluidization process to form the stabilized NE (**Figure 1.2B-C**)[20,21,22]. While this method may be relatively simplistic to implement, ligands tested often require a lengthy synthetic preparation and must be robust enough to withstand the shear forces imposed by the microfluidizer. Post-emulsification is a technique that conjugates the ligand to the surface after the

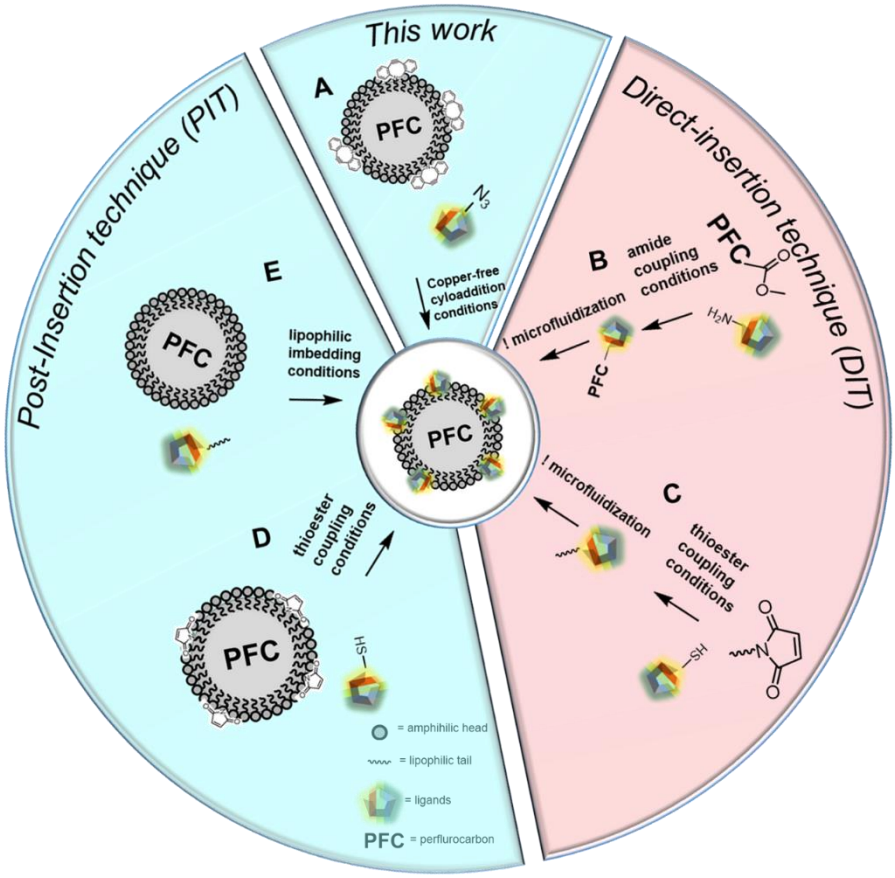

microfluidization procedure is complete (**Figure 1.2D-E**)[23]. This requires chemical modification of the surface of the particles to introduce functional groups, *e.g.,* amine, carboxyl, sulfhydryl, etc. Often, sulfhydryl-based linker chemistry is implemented in NE

Figure 1.2. Summarization of the various strategies used to functionalize PFC NE for ligand conjugation.

conjugation for the formation of covalent thioester bonds between maleimide and cysteine groups without the need for metal-catalysts. However, there are reported limitations with this strategy, such as the maleimide-linked products being particularly sensitive to hydrolysis and the chemistry optimally performs in inert atmospheres[24]. Functionalized PFC-NE have been shown to be stable in proper storage conditions and to bind successfully to targets[25,26].

1.4 This work

We demonstrate a copper-free click chemistry strategy commonly known as strain-promoted alkyne-azide cycloaddition (SPAAC) to facilitate NE-PFC conjugation (**Figure 1.1E**). This technique is ideal for occurring in mild reaction conditions and its low potential for cross-reactivity[27]. SPAAC has been used successfully for a variety of biological applications, such as live-cell imaging, radioisotope labeling, and surface modification[28,29,30,31,32,33]. We modify the dibenzocyclooctyne succinimide (DBCO-NHS) linker to have a lipid tail, dioctadecylamine, in order to facilitate incorporation to the perfluorocarbon nanoemulsion lipid shell and present the reactive cyclooctyne on the surface of the particle.

In this work, we sought to increase PFC nanoemulsions' affinity for M1 or M2 subtypes by attaching receptor-specific ligand, to the emulsion surface. The high density of PFC at the core of the emulsion droplets allows simple identification of ^{19}F nuclei in NMR or MRI imparting little or no cytotoxicity *in vivo*[34]. The outermost layer of nanoemulsion (*i.e.,* surfactant layer) is composed of phospholipids where amphiphilic molecules can be incorporated to functionalize the droplet surface for conjugation of biologically relevant ligands. Since the use of sulfated-dextran (SD) has reported affinity

to the M2 phenotype distinguishing scavenger receptor A1 (SR-A1)[35,36], we proposed to add azide functionality to the charged polymer and conjugate it to the surface of PFC-NE. With this, we may optimize conditions for PFC labelling to target M2 macrophages to assay TAMs *in vivo* with ^{19}F MRI.

Chapter 2. Characterization of Click-ready DBCO-PFC-NE

2.1 Methodology

Scheme 2.1. Synthesis of DBCO-PFC-NE

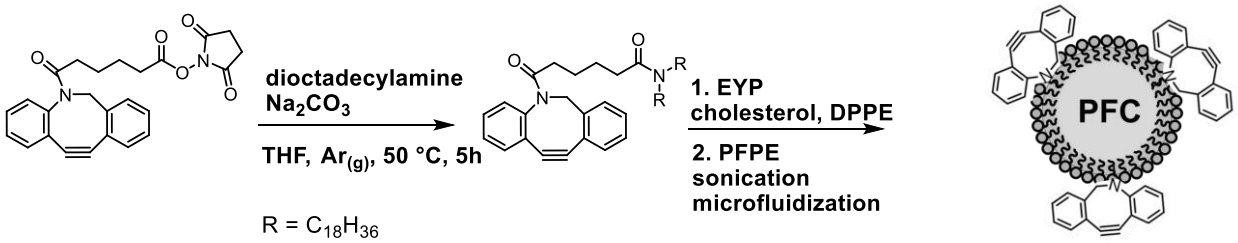

2.1.1 Nanoemulsion Preparation

In a 10-mL dram vial, the lipid layer was formed by adding 95 mg egg yolk phospholipids (EYP, Sigma-Aldrich), 20 mg cholesterol (Avanti Polar Lipids, Alabaster, AL), 2.4 mg 1,2 dipalmitoyl-sn-glycero-3-phosphoenthanolamine (DPPE, Avanti), and 5.45 mg DBCO-lipid and dissolved in 2 mL chloroform. The lipid solution was then dried under a gentle stream of argon gas and constant rotation to ensure an even layer on the glass surface. The sample was dried overnight under high vacuum. The next day, 122 mg D-mannitol (Sigma-Aldrich) and 4.5 mL of miliQ water were added to the dried lipid film and subsequently vortexed for 30 s and sonicated for 2 mins (Omni Ruptor 250 W, 30% power, 2 min Omni international, Kennesaw, GA). Then 2.136 g perfluoropolyether (PFPE, Flobin, Solvay) and 180 mg Cremophor (Sigma-Aldrich) were added to the solution, followed by a brief vortex and sonication for 2 mins. The crude solution was passed 5 times through the LV1 microfluidizer (Microfluidics, Newton, MA) operating at 30,000 psi. The emulsion was filtered through a 0.22 µm Supor membrane (no. 4187, Pall, Port Washington, NY) into sterile glass vials. Size characterizations were performed with dynamic light scattering (DLS, Malvern Zetasizer ZS, Malvern, PA). Fluorine concentration was determined by ^{19}F NMR spectroscopy (Bruker).

2.1.2 Fluorescent assay methodology

For quantification of reactive DBCO, DBCO-PFC-NE was reacted with Alexafluor 488 azide (AF488) in various conditions to produce its fluorescently labeled form (AF-PFC-NE). Fluorescence measurements were collected by Tecan reader (Infinite M200PRO, Morrisville, NC). Conditions tested included the following: (i) DBCO mol% ranges (0.2, 0.5, 1, and 5, n = 4), (ii) Reaction time at 2 hr, 24 hr, and 48 hr timepoints, (iii) AF488 concentration range (n = 3). Saturated fractions (maximum bound) were collected and content of AF488 determined by absorbance for each of the selected DBCO mol% ranges. The amount of AF488 clicked to the surface was calculated from standard curve. The ratio of reactive DBCO compared to total DBCO added was determined by equation (1). Since AF488 and DBCO are equimolar based on the click reaction, concentration of AF488 ($[AF488]$) was equated to the reactive DBCO concentration ($[DBCO]_r$). Lastly, the DBCO starting material ($[DBCO]_T$) is compared to its $[DBCO]_r$ using Eq. 1 to yield the percentage of clicked ratio of reactive DBCO to total available in percent (R_{DBCO}). Differences in clicking efficiency can also be identified by comparing R_{DBCO} values across DBCO mol%.

$$R_{DBCO} = \frac{[DBCO]_r}{[DBCO]_T} \times 100\% \quad (1)$$

$[AF488]$	Determined oncentration of AF488 in µmol/L
$[DBCO]_r$	Determined concentration of reactive DBCO residues on NE surface in µmol/L
$[DBCO]_T$	Total concentration of DBCO available in solution
R_{DBCO}	Ratio of reactive DBCO to total available in percent
a	Insufficient data for calculation

2.2 Testing the parameters of DBCO-PFC-NE

2.2.1 Characterization and kinetic stability of DBCO-PFC-NE

We describe a synthetic scheme for DBCO-PFC-NE to allow for the click-and-go utility. The preparation of unfunctionalized PFC-NE has been well characterized for its pharmacokinetic properties and shows good stability and biocompatibility[37], so the synthesis of DBCO-PFC was an adaptation to this procedure. Based on previous accounts, dioctadecylamine is commonly used as a vehicle for lipid insertion into the nanoemulsion formulation[38]. Perfluoropolyether (PFPE) was selected for the core of the NE due to the large single peak that appears in ^{19}F NMR which facilitates higher sensitivity in ^{19}F MRI[39,40].

The DBCO-NHS reaction with dioctadecylamine produced the amide-linked product in 90% yield (**Scheme 2.1**). The DBCO-lipid was then incorporated into the lipid formulation at various mol% in relationship to the total moles of egg yolk phospholipid (EYP) content. Testing a range of mol% DBCO gave us insight into whether DBCO load perturbs physiochemical properties of the NE (e.g. size, stability, dispersity, etc.). In addition, it evaluates any differences in ligand coupling efficiencies for different % DBCO content. The minimum DBCO introduced was based on previous studies which showed

Table 2.1. Hydrodynamic size diameters and PDI values of DBCO-PFC-NE

	Size (d.nm)		PDI	
Sample	mean	SD	mean	SD
PFC-NE	165.5	2.5	0.109	0.020
0.2 mol% DBCO-PFC-NE	162.5	0.5	0.124	0.018
0.5 mol% DBCO-PFC-NE	166.7	2.7	0.134	0.013
1 mol% DBCO-PFC-NE	168.2	1.3	0.127	0.023
5 mol% DBCO-PFC-NE	167.8	1.7	0.134	0.003
χ^2	0.1		0.021	

that 0.5 mol% of ligand attached to NE provided optimal uptake[20]. **Table 2.1** summarizes size and polydispersity index (PDI) for unmodified PFC-NE and 4 different mol % of DBCO addition. There are non-significant changes as a result of increasing DBCO concentration for both size, X^2 (1, n = 3) = 0.10, p = .30 and PDI, X^2 (1, n = 3) = 0.02, p = .49, indicating that the addition of the DBCO-lipid did not perturb particle formation or size.

To assess if DBCO-lipid insertion introduced any instability to the PFC, size changes over time were compared against an unmodified PFC-NE control. Incubation conditions were selected to simulate the effects of long-term storage in either storage or *in vivo* conditions on the nanoemulsions. The methodology used here is seen in previous reports wherein each nanoemulsion is measured in water (**2.1a**) or serum (**2.1c**) (5% FBS

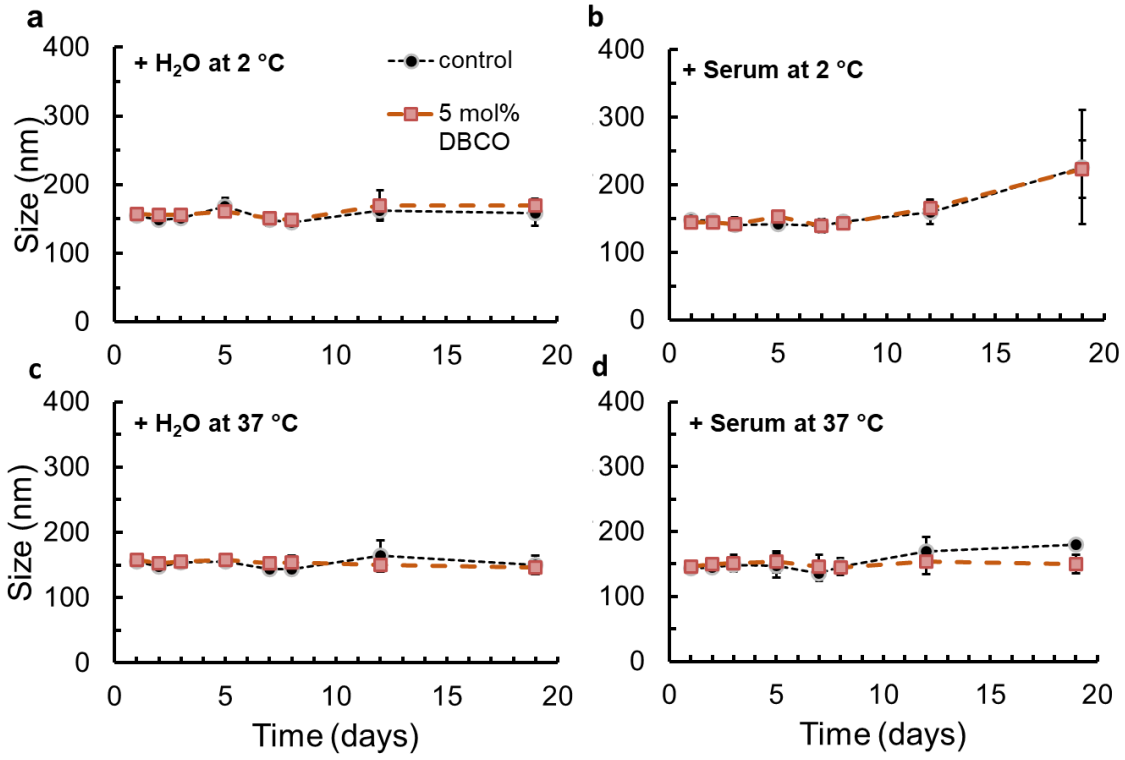

Figure 2.1. DLS results for droplet size changes over 19 days for PFC NE (control) and 5 mol% DBCO NE under various conditions (n = 3). Error bars reflect the standard deviation between three emulsion batches **a**) Both NE types were stored in miliQ water and 2 °C. p value = .182. **b**) Both NE types were stored in DMEM with 5% FBS and 2 °C. p value = .954. **c**) Both NE types were stored in miliQ water and 37 °C. p value = .524 **d**) Both NE types were stored in DMEM with 5% FBS and 37 °C. p value = .776

in DMEM) at 2 °C, which has been previously determined to retard the decomposition of NE (**Figure 2.1a**). To simulate blood plasma-like conditions, PFC-NE were incubated in 5% FBS -containing media at 37 °C (**Figure 2.1b**) and at 37 °C in water (**Figure 2.1d**).

The results comparing the variances show a non-significant change in size between the control and DBCO-PFC (**Figure 2.1**, two-tailed unpaired *t*-test). NE incubated at 37 °C, shown in **Figure 2.1c** and **2.1d** show an increase in emulsion size after 3 days which is characteristic of reported decomposition trends for nanoemulsions i*n vivo*[41]. Therefore, we concluded that the DBCO-PFC-NE exhibited similar stability properties to the unmodified PFC-NE reported in our previous studies[37].

2.2.2 Clicking efficency fluorescent assay

In order to understand the conjugating capacity of the particles and efficiency of the click reaction, DBCO-PFC-NE were reacted with Alexa Fluor 488 azide (AF488, $\lambda_{ex/em}$= 494/517 nm) and efficiency of coupling was determined by absorbance spectroscopy. Bound and unbound ligand, were distinguished through differing elution profiles through a size-exclusion separation column (Sephadex G50, Sigma Aldrich). In this system, the larger particles such as AF-PFC-NE eluted faster (**Figure 2.2**, fractions 1-10) while free AF488 eluted later (**Figure 2.2**, fractions 15-30). The range of AF488 used for all emulsions was 50 – 200 µM in order to assess changes in binding capacity over the mol% DBCO range.

As summarized in **Figure 2.2**, the absorbance signal for bound AF488 (fractions 4-6) appeared after the addition of 0.5 mol% DBCO and increased in amplitude as the % DBCO added increased (**Figure 2.2c**), while the peak for unbound AF488 (fractions 23-26) decreased. As expected, the higher mol% DBCO concentrations (**Figure 2.2d** and **2.2e**) showed an increase in AF488 conjugation effectiveness with 5 mol% DBCO

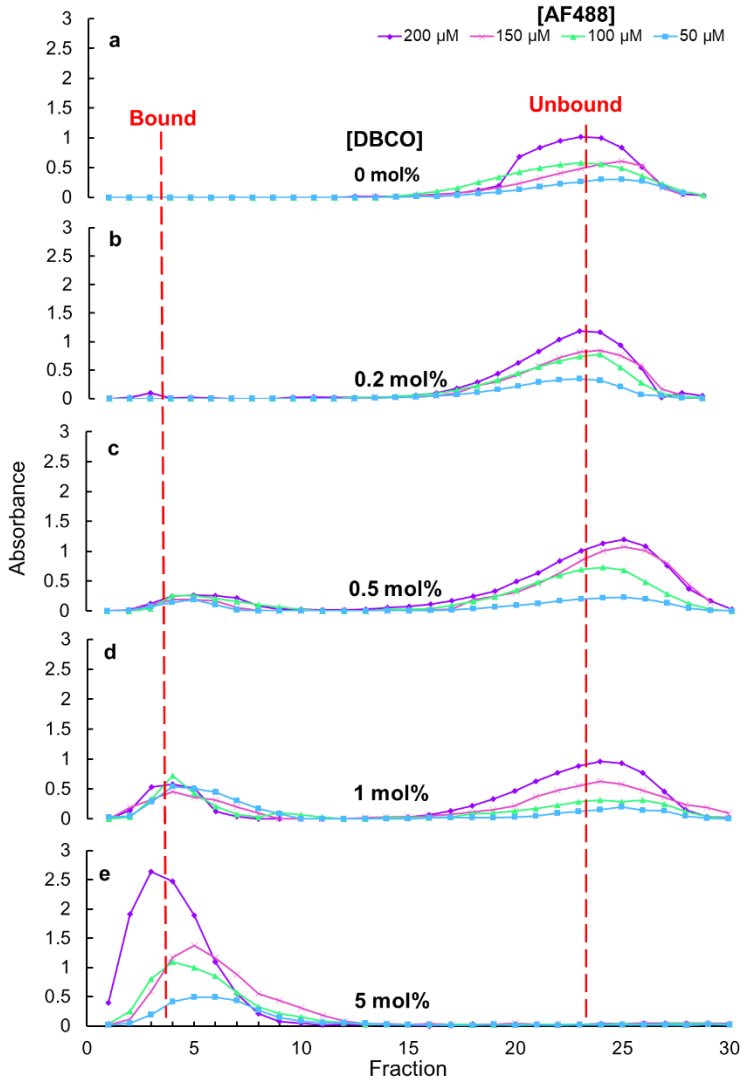

Figure 2.2. Elution profile of DBCO-PFC-NE reacted with AF488 azide separated by size-exclusion column (sephadex G50). Absorbance measured with a Tecan plate reader (Infinite M200PRO, Morrisville, NC) after 24 hr reaction time. PFC concentration was normalized for 200 mg/mL

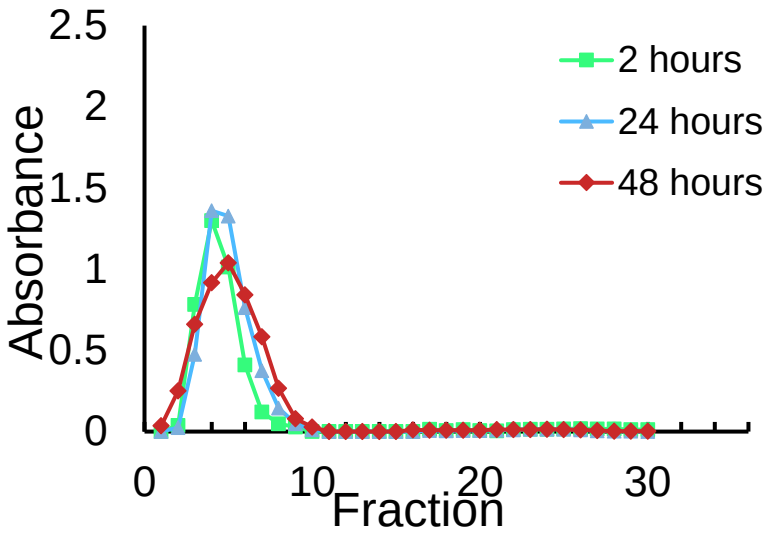

Figure 2.3. Elution profile of 5 mol% DBCO-PFC-NE reacted with 130μM AF488 azide for several periods of time at room temperature. *n* = 3 per time condition.

displaying completely bound ligand with no remaining unbound. This suggests that the binding capacity of the NE has been reached or exceeded. In order to determine the most effective reaction time for 5 mol% DBCO-PFC-NE, and the click reaction was allowed to proceed for 2 hr, 24 hr, and 48 hr. As shown in **Figure 2.3**, it is likely that most if not all azide is consumed after 2 hours. Quantitative statistical assessment of bound versus free ligand agrees showing no statistical differences between 2 hr, 24 hr, and 48 hr reaction periods (*p* value = .456).

The data in **Figure 2.2** was analyzed for relative clicking efficiency (**Figure 2.4**). The figure is a simplified over-view which describes the work-flow performed in order to quantify the important parameters of the reaction such as number of reactive DBCO residues (*[DBCO]r*) and the DBCO-clicking rate (R_{DBCO}) which can be derived by from the ratio of reactive DBCO to total DBCO starting material (SM). Our process required the collection of the bound fractions (typically fractions 1-10) wherein [AF488] present on the saturated DBCO-PFC-NE (*n* = 4) was quantified by an AF488 standard curve (see section 2.1.2 for detailed methods). All DBCO concentrations except for 0.2 mol% DBCO were

assessed due to the limited fluorophore present for detection even with fluorescence spectroscopy. **Figure 2.4** illustrates how the fractions from bound region at each mol%

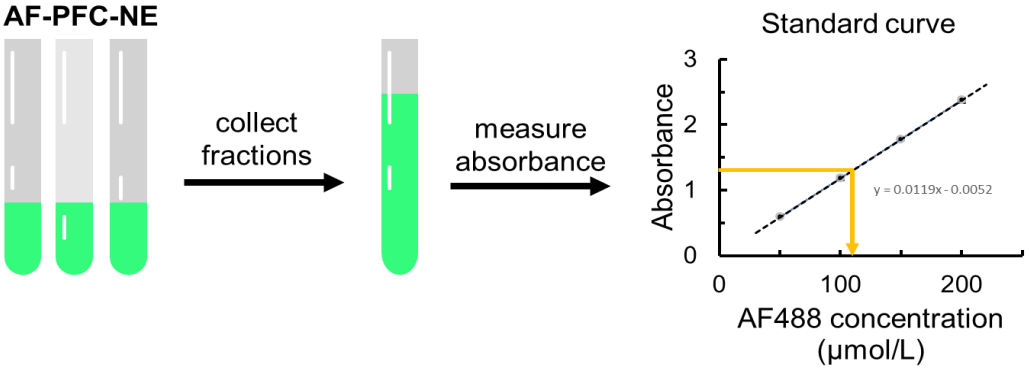

DBCO (mol%)	$[DBCO]_r$ (µmol/L)	R_{DBCO} (%)
0.2[a]	-	-
0.5	12.6 ± 3.3	11.6 ± 5.2
1	41.9 ± 12.3	19.3 ± 9.7
5	234.9 ± 16.5	21.6 ± 2.6

$$[AF488] = [DBCO]_r$$

$$R_{DBCO} = \frac{[DBCO]_r}{[DBCO]_T} \times 100\% \qquad (1)$$

$[AF488]$	Determined oncentration of AF488 in µmol/L
$[DBCO]_r$	Determined concentration of reactive DBCO residues on NE surface in µmol/L
$[DBCO]_T$	Total concentration of DBCO available in solution
R_{DBCO}	Ratio of reactive DBCO to total available in percent
a	Insufficient data for calculation

Figure 2.4. Work-flow for fluorescence quantification assay

DBCO assessed were compared against a calibration curve to help determine *[DBCO]r* and R_{DBCO} values. The results displayed statistically significant increases in *[DBCO]r* showing a 3.3 fold increase from 0.5 to 1 mol% and a 5.6 fold increase from 1 to 5 mol%. R_{DBCO} values represent a % yield of sorts for reactive DBCO compared to the SM DBCO added. The highest efficiency of clicking was found for 5 mol % DBCO with 21.6 ± 2.6 % reactive DBCO relative to starting material DBCO added. In the future, work can be done to increase the efficiency by exploring other lipid tails attached to the DBCO to improve positioning of DBCO at the surface of the NE after the emulsification process. The 5 mol% PFC-NE were used for the *in vitro* and *in vivo* assays.

Chapter 3. Biological Studies of Click-ready DBCO-PFC-NE

3.1 Methodology

3.1.1 RAW 246.7 cells.

Frozen RAW 264.7 cells (Abcam), were thawed and maintained in DMEM x1 media containing 5% FBS in T75 flasks (Sigma). Incubated in 37 °C at 35% CO_2.

3.1.2 In vitro cell cytotoxicity assay

RAW 264.7 cells were plated at a density of 100,000 cells per well (36 wells total) in clear bottom 6-well plates (Corning, Inc., Corning, NY) and were allowed to adhere. Wells (n = 3, per condition) received: (i) PFC-NE dose range (2-10 mg/mL, control), (ii) DBCO-PFC-NE dose range (2-10 mg/mL), or (iii) AF-PFC-NE dose range (2-10 mg/mL). After overnight incubation (16 hours), cell-plates were washed twice with 1% sterile PBS and incubated with 0.25% trypsin resuspension buffer (2 mL per well) for 5 min. Then DMEM media is added (8 mL per well) and extracted into a 10-mL sterile Falcon tube. An aliquot of suspended cells (10 µL) is mixed with trypan blue staining (10 µL) in a 96-well plate and assayed with a Countess II FL Cell Counter (Life Technologies). The relative cell cytotoxicity was obtained by normalization to the non-dosed control.

3.1.3 Paw Inflammation Model

All animal work was approved through the University of California, San Diego, Institutional Animal Care and Use Committee (IACUC). In vivo studies were performed to confirm colocalization of AF-PFC-NE ^{19}F and fluorescence signals to the site of inflammation (the right paw). Female mice (n = 3) mice 4-6 weeks of age (ICR CD-1, Envigo) received subcutaneous injections in the right paw, each containing 0.5% carrageenan solution in 0.9% saline solution. After 1 hour, each mouse received 112

mg/mL AF-PFC-NE in TRIS-HCL buffer (2% propylene glycol) by intravenous (IV) injection via tail-vein. Once inflammation was established by measuring paw sizes,(~4 mm size) after 24 hours, fluorescence and ^{19}F signals were measured by bioluminescence imaging (BLI) and ^{19}F MRI respectively.

3.1.3 Bioluminescence imaging (BLI)

All mice underwent serial fluorescence detection using BLI (IVIS, Perkin Elmer, Waltham, MA) one hour after receiving AF-PFC-NE. Prior to BLI, mice received hair removal with Nair treatment to reduce background autofluorescence. A white-light body surface image was collected, followed by an image of the spatial distribution of photon counts rendered in pseudo-color, which was overlaid onto the surface image. Quantitative analysis of the radiance flux (photons/s) was performed with the Living Image Software (Perkin Elmer, Waltham, MA) by defining identical regions of interest covering the left (control) and right paws. Following measurements, paw-sizes were measured using a caliper.

3.1.4 Magnetic Resonance Imaging (MRI)

Mice were anesthetized with 1–2% isoflurane in O_2 and positioned an 11.7 T Bruker BioSpec preclinical scanner with a dual-tuned $^{1}H/^{19}F$ birdcage volume coil. Animal temperature was regulated, and respiration was monitored during scans. A reference capillary with the AF-PFC-NE was positioned in the image (field of view) FOV. Lower body ^{1}H anatomical images were acquired using the (rapid acquisition with relaxation enhancement) RARE sequence with TR/TE = 1250/15 ms, RARE factor 6, matrix 256 × 192, FOV 40 × 30 mm, slice thickness 1 mm, 20 slices, and 6 averages. Lower body ^{19}F

images were also acquired using a RARE sequence with parameters TR/TE = 1000/20 ms, RARE factor 8, matrix 48 × 320, FOV 40 × 30 mm, slice thickness 2 mm, 10 slices, and 300 averages. The total number of fluorine atoms per voxel in tumor regions were estimated directly from 3-D interpolation of regions of interest (ROI) by segmenting around relevant ^{19}F signals (right paw, left paw, and liver), and ROI voxel intensities were displayed as histograms (**Figure 3.2**). For display, ^{19}F images were adjusted to remove background noise, and $^{1}H/^{19}F$ renderings were performed in VivoQuant™ (Invicro) by overlaying ^{1}H (grayscale) and ^{19}F (hot-iron scale) slices.

3.1.5 Immunohistochemical analysis

After imaging, the right and left paws of each animal were embedded in optimal cutting temperature (OCT) compound (Sakura Finetek USA, Inc., Torrance, CA) and stored at −80 °C. All tissues were cryosectioned (CM1950, Leica Microsystems Inc., Buffalo Grove, IL) at 10 μm thickness. Sections were fixed with 4% paraformaldehyde, stained for macrophage cells using Alexa Fluor 647 anti-rabbit mannose receptor (ab64693, 1:500 dilution, donkey anti-rabbit, Abcam) and for nuclei using Hoechst dye (1:500) and then mounted. Fluorescence images were acquired on an Axiovert 40 CFL microscope (Zeiss, Thornwood, NY) using a ×5 objective. Confocal images were acquired on a Leica SP5 2 confocal system with a Leica DM 6000 CFS microscope and a ×63 immersion objective.

3.1.6 Statistical analysis

Measurements are presented as mean ± SD. We performed unpaired T-tests with unequal variances to compare in vivo groups. Two tailed *p* values <0.05 were considered statistically significant.

3.2 *in vitro/in vivo* results of DBCO-PFC-NE

3.2.1 Cytotoxicity of DBCO-PFC-NE

The cytoxicity of DBCO-PFC-NE was assessed on RAW 246.7 cells. Approximately 1 million cells were incubated with 2-10 mg/mL doses of DBCO-PFC-NE, AF-PFC-NE, and PFC-NE control (*n* = 3) overnight at 37 °C. Viability was assessed by trypan blue live/dead staining. As shown in **Figure 6**, there was no statistically significant difference from control for any concentration tested for either DBCO-PFC-NE or AF-PFC-NE (*p* values = .528, .583, .914).

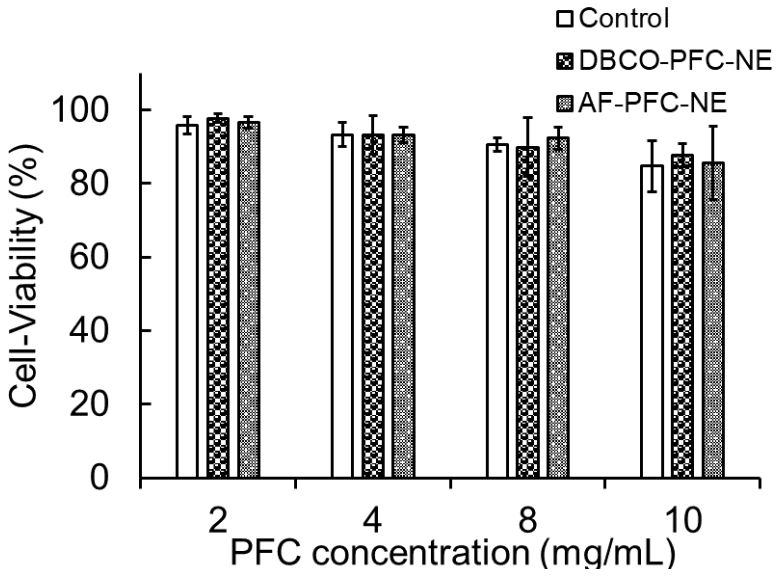

Figure 3.1. Cytotoxicity assay dosing RAW 246.7 macrophages with various concentrations of click-ready (DBCO-PFC-NE) and fluorescent click conjugated (AF-PFC-NE) particles (*n* =3).

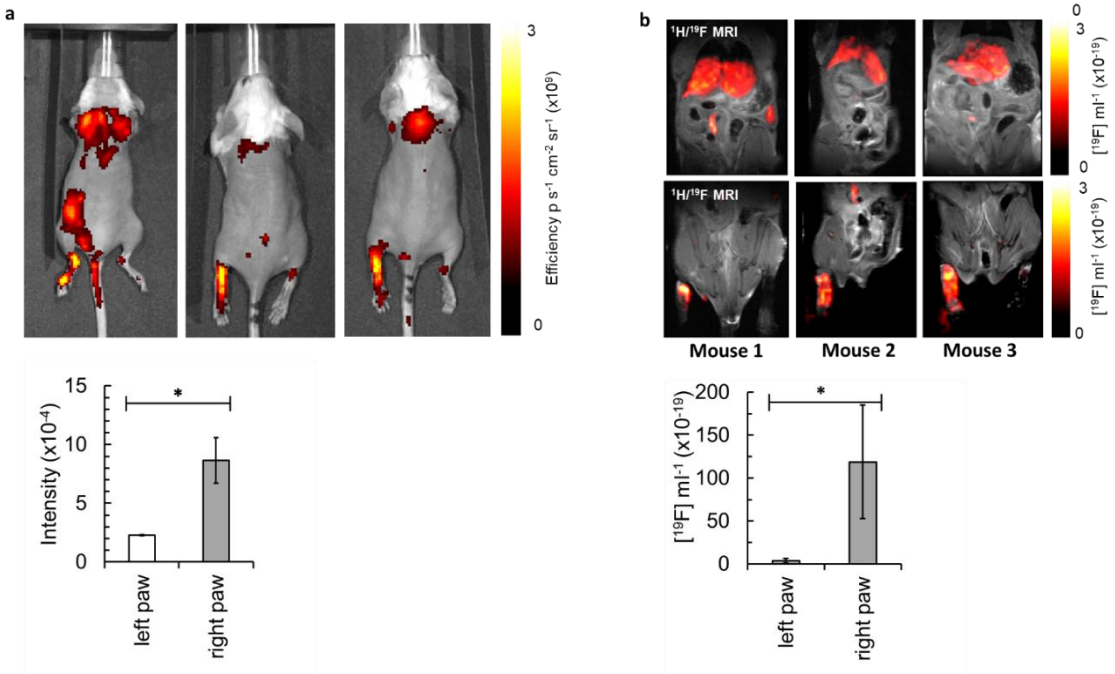

Figure 3.2. In vivo BLI and $^{1}H/^{19}F$ MRI overlay showing localization of i.v. injected AF-PFC-NE in paw inflammation CD-1 mice. (a) BLI images of paw inflammation CD-1 mice 24 h post 5% carrageenan injection (*n* = 3) and fluorescence intensity presented on a 'hot iron' scale bar. (b) Composite $^{1}H/^{19}F$ MRI images of torso and abdomen of injected mice showing ^{19}F signal represented by the 'hot iron' scale. Quantification confirmed higher uptake of the particles in the injured right paw. (b,top) Torso visualization showed signal in other immune cell-dense regions as seen in liver and spleen. (b, bottom) Abdomen visualization showing high signal in inflammation in the injected leg, which was confirmed by quantification through ^{19}F NMR spectroscopy.

3.2.2 Imaging AF-PFC-NE in MRI/BLI *in vivo*

To evaluate the multimodal efficacy of click-labeled nanoemulsions to display overlapping fluorescence and ^{19}F signal in vivo, Band $^{1}H/^{19}F$ MRI signals were measured after intravenous (i.v.) injection of AF-PFC-NE (112 mg/mL) into the tail-vein of CD-1 mice with paw inflammation induced by carrageenan injection. PFC agents have been shown to be internalized by immune cells by endocytosis in multiple studies[42]. It was expected that the AF-PFC-NE fluorescence and ^{19}F signals would colocalize in the induced paw. **Figure 3.2a** shows whole-body images of mice 24 h after injection of 5% carrageenan solution in the right paws (*n* = 3). Since only the right-paw was injected with the

inflammation solution, the left-paw was measured as control. Images showed bright emission in the right paw that was significantly higher than the left paw (p = .009, t-test). The mice also showed varying degrees of background signal due to skin irritation caused by the hair removal procedure; these were evident as signal behind the head of all 3 mice and on the left side of the torso on the mouse on the left. MRI measurements detected large ^{19}F signal in the right paws of each mouse with significant difference between left and right paws (p = 0.039, t-test). Combined, the BLI and MRI images show that we can observe AF-PFC-NE fluorescent and F-19 signals colocalize to the inflamed regions in this paw inflammation model.

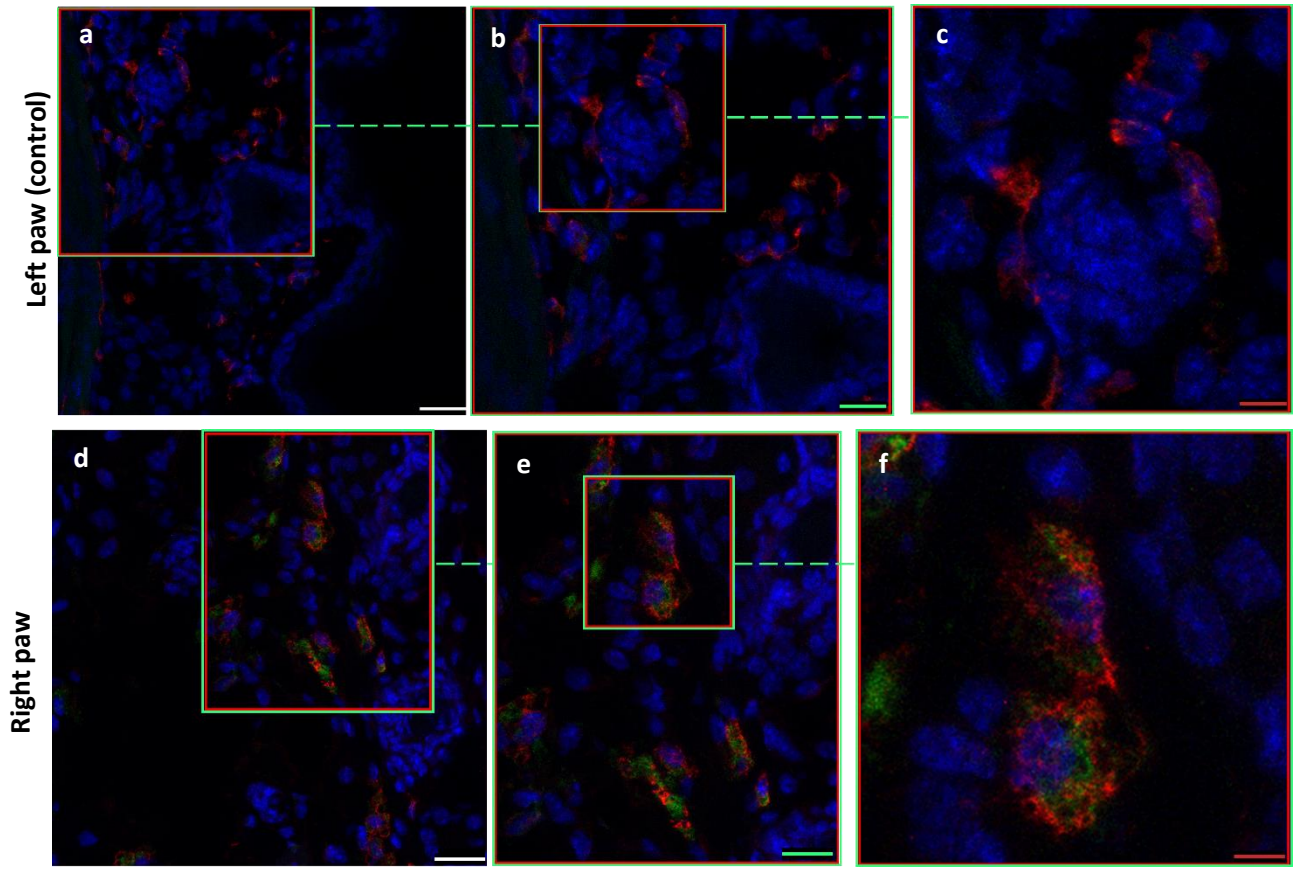

Figure 3.3. Confocal images of inflamed paw tissue. Overlay of DAPI (blue), mannose receptor (red, ab6493, Abcam), and AF488 (green) is shown. (Top) Panels a, b and c show progressive zoomed image of IHC stained left paw slice with macrophage presence and absence of AF488. (Bottom) Panels d, e, and f show progressive zoomed in views confirming cytoplasmic localization of AF488-PFC-NE in macrophages. Scale bars are in 0 - 25 µm (white), 0 – 12 µm (green), and 0 – 6 µm increments.

To confirm that the NE localized to inflammatory cells, immunohistochemical (IHC) analysis was performed on the right and left paws and imaged with confocal microscopy. From previous reports demonstrating IV injections of plain PFC-NE, the plain nanoemulsions have a tendency for endocytic uptake by immune cells including macrophages in areas of inflammation. Macrophages were stained for mannose receptors using Alexa Fluor 564 secondary antibody (red) and co-localization between mannose positive macrophages (red) and AF-PFC-NE (green) was shown. **Figure 3.3** is a representative confocal image for the right paw. Several macrophages are evident with strong red signal, overlapping with the cytoplasmic green signal from AF-PFC-NE. IHC analysis of the left paw showed presence of macrophages, however no presence of AF-PFC-NE, which supports that the DBCO-PFC-NE preferentially migrated and localized in the inflamed right paw but not the contralateral control (left paw). One possible explanation for seeing macrophages in both paws is that there are macrophages all throughout the biological system. Regarding our observations of both paws, this shows a successful aggregation of AF-PFC-NE into the inflamed paw as observed with ^{19}F nuclei via MRI and fluorescence via BLI.

Chapter 4. Preliminary Selectivity Assessment of SD-PFC-NE

4.1 Methodology

4.1.1 Synthesis and Characterization of SDA

Scheme 4.1. Synthesis of SDA

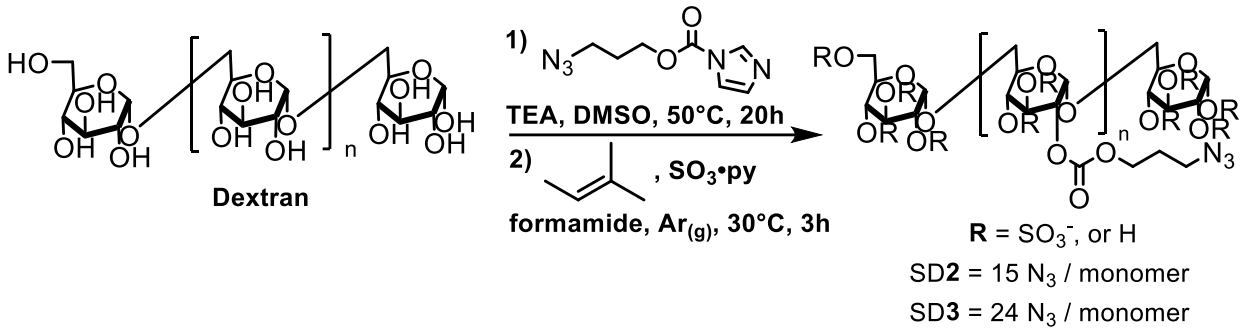

Sulfated dextran (SD) has been reported to have strong affinity for the scavenger receptor A (SRA) expressed uniquely by M2 macrophages. SD azide functionalization (SDA) was performed in a two-step synthesis using reported methods (**Scheme 4.1**). First 3-azidopropanyl carbonlyimidazole (AP-CI) was added to a dextran solution dissolved in DMSO at 50 °C for 20 hours. The product was purified by dialysis for 72 hours and lyophilized to be added to a solution of formamide, 2-methyl-2-butene, and sulfur trioxide pyridine. The product was then purified by dialysis and produced SDA in 80% yield and characterized by ^{1}H NMR spectroscopy. We varied equivalents of AP-CI to determine if azide per ligand substitution affects conjugation with the nanoemulsion. SDA versions with 5, 15 (SD2), and 24 (SD3) azides per dextran 10kDa monomer were produced. Estimation of azide substitution was determined by Fourier-transform infrared spectroscopy (FTIR).

4.2 Results and discussion

4.2.1 Optimization of SDA attachment

Quantification of SDA attachment offers a unique challenge that may be solved through several methods. We chose to label the SDA types with a small amount of

fluorescent alkyne to fluorescently identifying clicking after size exclusion separation. Sulfo-Cy5 was chosen due to its high polarity to deter it from simply sticking to the lipophilic emulsion surface. A copper-catalyzed click reaction was then performed by reacting sulfo-Cy5 in an aqueous solution of SDA, MOPS buffer, tris (benzltriazolymethyl) amine (THPTA), sodium ascorbate and $CuSO_4$ for 1.5 hours under $Ar_{(g)}$ (**Figure 4.1A**)[43]. The product was then purified with size -exclusion chromatography (Sephadex-G50) followed by lyophilization to determine mass and absorbance for its ratio of fluorophore to SDA.

DBCO-PFC was saturated with the two Cy5-SD types (SD**2** and SD**3**) and separated by size exclusion chromatography (Sephadex G200). The bound fractions collected were measured for Cy5 concentration by absorbance (λ = 649 nm) and adjusted by their Cy5 per monomer ratios to represent the SDA ligands. $Bound_{max}$ mol% represents the ratio of ligand to total DBCO (**Figure 4.1B**). For reference, AF488-azide is the control which requires 33.3 mol% to saturate the nanoemulsion. It appears that more SD**3** ligand can bind to DBCO-PFC than SD**2** (comparing 42.5 to 20.4 mol% respectively). SD**3 has** increased probability for reaction by having more azides per monomer, and a greater coupling ratio is observed as a result. With increased attachment of SD**3** comes a loss in azide efficiency with excess 5 eq. (azide per DBCO). These results will assist in selecting reasonable concentrations to assess whether SD**2** or SD**3** promotes greater cellular uptake.

4.2.2 Optimization of SD-PFC-NE uptake in vitro

Unstimulated macrophages were used as a preliminary strategy to rapidly assess suggested dose and labelling concentrations of SD-PFC. Assays were performed by co-incubating the RAW 246.7 macrophages, an immortalized, adherent cell-line, with Dulbecco's Modified Eagle Media (5% fetal bovine serum) and the PFC nanoemulsions. Following the incubation period, two washes were performed with phosphate buffer solution to remove cellular debris and free PFC. A small amount of trypsin as added to suspend cells in media for cell counting. After centrifugation and the addition of lysis buffer, a fraction of cells was extracted for ^{19}F quantification via ^{19}F NMR using a trifluoracetic acid reference. All analyses were performed in triplicate.

The first assay performed compared the effects of the nonfluorescent SDA types at fixed concentrations of SD and PFC and their uptake in cells for 10 hours (**Figure 4.2A**, top). In comparison with the control, plain PFC nanoemulsions (without **1**), both SD**2** and

B

Sample	Azides per ligand	Bound Cy5 (mol%)	$Bound_{max}$ (mol% ligand)	$Bound_{max}$ (eq. azide/DBCO)
AF488	1	-	33.3 ± 1.3	0.33 ± 0.01
SD**2**	15	22	20.4 ± 1.0	3.06 ± 0.15
SD**3**	24	24	42.5 ± 1.5	4.93 ± 0.18

Figure 4.1. Fluorescent quantification of SDA attachment. (A) Sulfo-Cy5 attachment to SD (2,3) via Cu(I) catalyzed click reaction 4: SD(2,3) (1 eq.), sulfo-Cy5 (2 eq.), $CuSO_4$ (1 eq.), THPTA (2.5 eq.), Na-ascorbate (20mM), and MOPS (50 mM) in water for 1.5h. (B) Maximum binding of ligands to DBCO-PFC with AF488, SD2, and SD3 in 5 mol% 1. Bound Cy5 mol% is the ratio of µmol Cy5 to µmol dextran monomer. $Bound_{max}$ mol% ligand ratio of µmol ligand to µmol DBCO. $Bound_{max}$ eq. azide/DBCO is ratio of µmol azides to µmol DBCO. Quantification was determined by absorbance spectroscopy after separation with size exclusion chromatography (λ = 649 nm, *n* =3).

3-PFC showed a significant increase in ^{19}F uptake. High viability was also observed for each, indicating that SDA conjugation did not significantly increase cytotoxicity **(Figure 4A**, bottom). These promising preliminary results showed higher uptake of macrophages of SD-PFC. However, the difference between SD**2**-PFC and SD**3**-PFC significant (*p* value < 0.05) which may be a consequence of the different azide distribution per chain for the two types (15 azides per ligand and 24 azides per ligand respectively). However, less SD**3** is required to saturate compared to SD**2** seen in the fluorescent assays indicates that more SD was incorporated at higher concentrations compared to SD**2**. As a result, SD**3** will be used in future cellular assays.

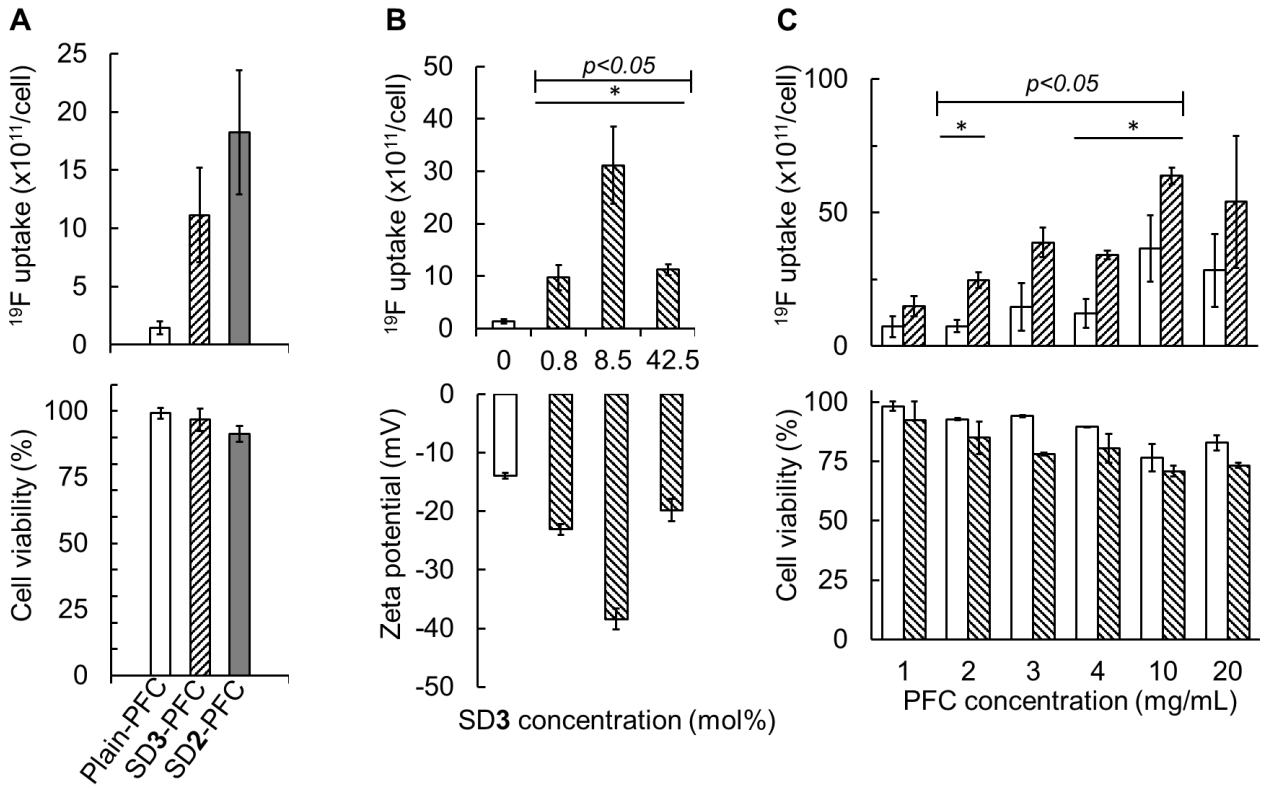

Figure 4.2. The effect of uptake due to SD-PFCs conjugation incubated with RAW 246.7 macrophages. (A) Cell uptake and viability varying SD-PFC types, 1 equiv of SD3 and SD3 (azide per DBCO) each, at 4 mg/mL PFC compared to plain-PFC after 10 h incubation (*n*=3, no significant differences noted between uptake and viability SD2 and SD3). (B) Cell uptake and zeta potential for SD3-PFC varying mol% SD3 after 18 h incubation (*n*=3). (C) Cell uptake and viability for varying doses of SD3-PFC based on mg/mL PFC compared to plain PFC control (white bars) (*n*=3).

In order to determine the optimal mol% SD**3** which promotes greatest uptake compared to plain-PFC nanoemulsions, another cellular assay was performed (**Figure 4.2B**, top). To complement the fluorescent assays, the same mol% concentration range of SDA was used with a fixed concentration of DBCO-PFC for 48 hours. Surprisingly, 8.5 mol% SD**3** had the highest ^{19}F uptake. This deviates from the assumption that ligand saturation leads to better uptake. Additionally, 8.5 mol% SD**3** has the most negative zeta potential out of the concentrations tested (**Figure 4.2B**, bottom). This was a curious result and we speculate that there was a reduction of sulfate presentation in its aqueous environment from increasing mol% SD**3**. The SRA binding-site has a high affinity for charged macromolecules which could explain the greater uptake of a stronger anionic

emulsion[35]. Nevertheless, these results indicate that 8.5 mol% SD**3** should be used for clicking to DBCO-PFC.

Lastly, a dose-response assay was conducted using SD**3**-PFC under the optimal conditions determined (**Figure 4.2C**, top). DBCO-PFC nanoemulsions had reacted with 8.5 mol% SD**3** for 48 hours and later incubated with cells in various doses of PFC. As expected, both the control and SD**3**-PFC showed an increase in uptake at higher concentrations until doses ≥ 10 mg/mL which then begun to display a subtle plateau in uptake. This is representative of the canonical sigmoidal uptake curve with increasing PFC. Cell viability appears to diminish with higher concentrations. It appears cells responded with better uptake and cell-viability between 2 mg/mL to 10 mg/mL SD**3**-PFC. In summary, the dose-response curve provides more evidence that SD**3** is a suitable ligand for assisting in the preferential uptake of PFC nanoemulsions in macrophages.

Chapter 5 Conclusion and Outlook

5.1 Limitations of current experiments

As mentioned in section 2.2.2, the DBCO-clicking yield (R_{DBCO}) at its best was reported at 21.6% (**Figure 2.4**) which may be the result of the lipid anchor used to modify the DBCO molecule. A possible explanation for this low result was mentioned to be attributed to the directional confusion of the DBCO-lipid embedding its reactive alkyne into the surfactant layer instead of being exposed in solution. One possible solution would be to increase the amphiphilicity of the DBCO-lipid by introducing a phosphate group separating the lipid-tail and the DBCO head group. The phosphate group would encourage the DBCO head group to be on the exterior of the molecule as the lipid-tail anchors itself in the surfactant layer as a result of the hydrophobic-effect during emulsification. If this works, we can expect to see an increase in the R_{DBCO} overall creating a more efficient reaction.

Another concern is that all prospective ligands are required to have the azide reactive group for attachment to DBCO-PFC-NE. Fortunately, due to the high demand of the azide functional groups for molecules, there are many methods reporting successful azide functionalization for a diverse range of molecuels (**Figure 5.1**)[44]. Since peptides are one of the most common targets of functionalization, several approaches have been developed for adding azide functionality is to utilize azide molecules with leaving-group N-hydroxysuccinimide (NHS) to perform the simple substitution reaction on either amine groups which is seen implemented in **Scheme 4.1**. Larger peptides are more difficult to modify due to the increased pressence of reactive lysine and cystine residues which can nonselectively react with NHS-azides. Fortunately, there is a strategy to circumvent this issue that uses unnatural amine acids (UUAs) in solid-phase peptide synthesis[45]. Since

we expect to modify peptides, antibodies, oligiomers, and small molecules for ligand conjugation, it is advantagous to consider these strategies.

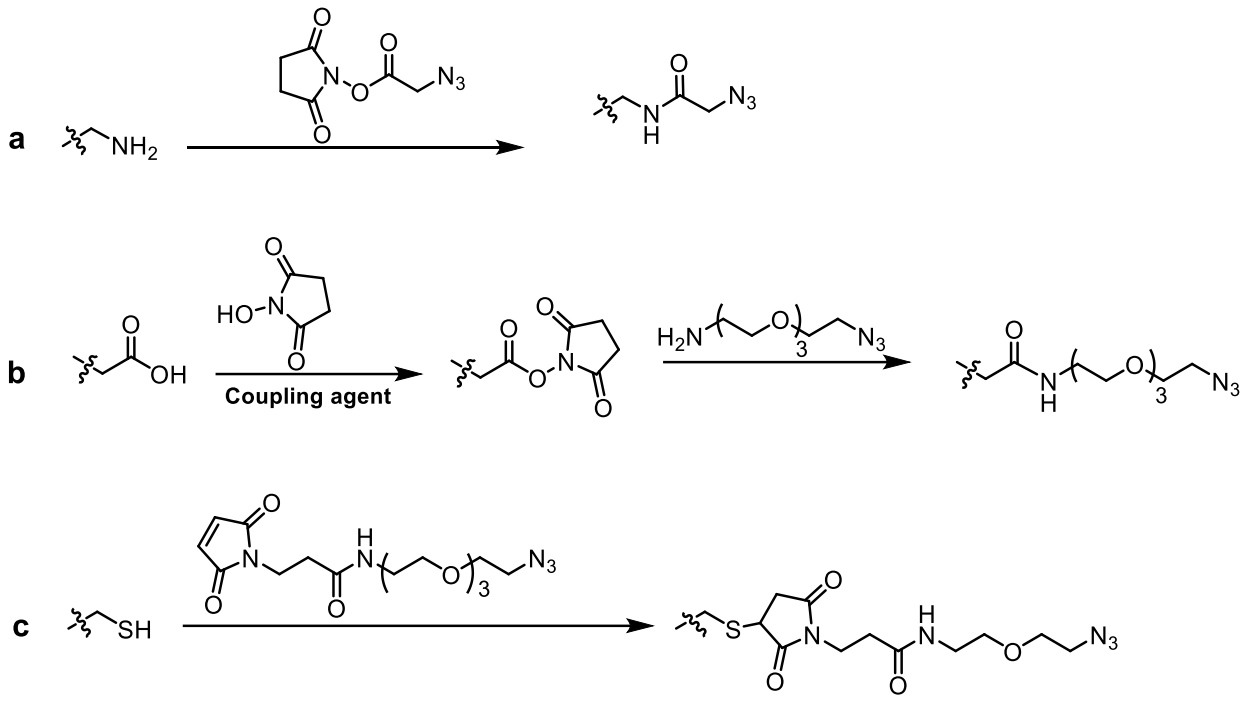

Figure 5.1. Summarization of various azide-modification strategies. **a**) Reaction scheme for functionalization of primary amines with NHS ester. **b)** Reaction scheme for azide functionalization of carboxylic acid using NHS ester, where the couple agent would be 1-ethyl-3-(dimethylamineopropyl)carbodiimide (EDC) or*N,N'*-dicyclohxylcarbodiimide (DCC). **c**) Reaction scheme for azide functionalization of a thiol using maleimide.

Another concern is the inherent stabililty of nanoemulsions to degrade under various conditions. Nanoemulsions are thermodynamically unfavorably systems which explains their common trend towards instability. For better or for worse, nanoemulsions have specfic rates for degredation depending on many factors, notably their sufactant composition and physical environment. However, as demonstrated in this thesis, there are methods to check some of the important properties for stability using DLS (**Figure 2.1**). In this way, the stability of future nanoemulsions can be characterizedusing this method.

5.2 Conclusion and future perspectives

To summarize, we report a novel bioconjugation method for PFC-NE that uses copper-free click chemistry to attach targeting ligands, and we demonstrate successful clicking of a fluorescent azide as proof-of-concept. Overall, the click modification shows excellent reactivity in the mild conditions using water and room temperature conditions. The clicked AF-PFC-NE product successfully display dual fluorescence and ^{19}F signals in the inflamed paw of the mouse model.

The selectivity of SD-PFC will be examined from uptake assays which isolate M1 or M2 macrophage proliferation. Utilizing the established protocols for M1 and M2 stimulation, we will incubate SD-PFC in both conditions and compare their uptake. If SD-PFCs show preferential uptake in M2 macrophages, then a competitive binding assay will be performed, which will measure its binding in the presence of free sulfated dextran to compete for binding sites. If these experiments are successful, we will conduct several MRI experiments visualizing and quantifying the bioaccumulation of SD-PFC injected in healthy mice and those with acute inflammation. These will compare whether the SD modified PFCs show significant differences compared to the control.

Click-ready PFC-NE have the potential to streamline preparations of PFC for molecular imaging by ^{19}F MRI. Simple coupling to azide-modified ligands would facilitate targeting strategies for many desired cell-types. The rapid click reaction and ability to click post-emulsification opens applications to ligands that are more sensitive to manipulation, and to harsh temperature and pressure conditions experienced during emulsification. The ready availability of many commercial, azide-functionalized ligands offers an accessible resource for biological laboratories and clinics to simply modify click-ready PFC with

targeting ligands of choice. This synthetic ease has the potential to facilitate wider adoption of ^{19}F MRI for molecular imaging by interested researchers.

References

(1) Dunn, G. P.; Old, L. J.; Schreiber, R. D. The Three Es of Cancer Immunoediting. *Annu. Rev. Immunol.* **2004**, *22* (4), 329–360. https://doi.org/10.1146/annurev.immunol.22.012703.104803.

(2) Qian, B. Z.; Pollard, J. W. Macrophage Diversity Enhances Tumor Progression and Metastasis. *Cell* **2010**, *141* (1), 39–51. https://doi.org/10.1016/j.cell.2010.03.014.

(3) Xue, J.; Schmidt, S. V.; Sander, J.; Draffehn, A.; Krebs, W.; Quester, I.; DeNardo, D.; Gohel, T. D.; Emde, M.; Schmidleithner, L.; et al. Transcriptome-Based Network Analysis Reveals a Spectrum Model of Human Macrophage Activation. *Immunity* **2014**, *40* (2), 274–288. https://doi.org/10.1016/j.immuni.2014.01.006.

(4) Murray, P. J.; Allen, J. E.; Biswas, S. K.; Fisher, E. A.; Gilroy, D. W.; Goerdt, S.; Gordon, S.; Hamilton, J. A.; Ivashkiv, L. B.; Lawrence, T.; et al. Macrophage Activation and Polarization: Nomenclature and Experimental Guidelines. *Immunity*. Cell Press July 17, 2014, pp 14–20. https://doi.org/10.1016/j.immuni.2014.06.008.

(5) Zhang, M.; He, Y.; Sun, X.; Li, Q.; Wang, W.; Zhao, A.; Di, W. A High M1/M2 Ratio of Tumor-Associated Macrophages Is Associated with Extended Survival in Ovarian Cancer Patients. *J. Ovarian Res.* **2014**, *7* (1), 19. https://doi.org/10.1186/1757-2215-7-19.

(6) Ramesh, A.; Kumar, S.; Brouillard, A.; Nandi, D.; Kulkarni, A. A Nitric Oxide (NO) Nanoreporter for Noninvasive Real-Time Imaging of Macrophage Immunotherapy. *Adv. Mater.* **2020**, *32* (24). https://doi.org/10.1002/adma.202000648.

(7) Sutherland, R.; Delia, D.; Schneider, C.; Newman, R.; Kemshead, J.; Greaves, M. Ubiquitous Cell-Surface Glycoprotein on Tumor Cells Is Proliferation-Associated Receptor for Transferrin. *Proc. Natl. Acad. Sci. U. S. A.* **1981**, *78* (7), 4515–4519. https://doi.org/10.1073/pnas.78.7.4515.

(8) Widera, A.; Norouziyan, F.; Shen, W. C. Mechanisms of TfR-Mediated Transcytosis and Sorting in Epithelial Cells and Applications toward Drug Delivery. *Adv. Drug Deliv. Rev.* **2003**, *55* (11), 1439–1466. https://doi.org/10.1016/j.addr.2003.07.004.

(9) Overman, M. J.; Modak, J.; Kopetz, S.; Murthy, R.; Yao, J. C.; Hicks, M. E.; Abbruzzese, J. L.; Tam, A. L. Use of Research Biopsies in Clinical Trials: Are Risks and Benefits Adequately Discussed? *J. Clin. Oncol.* **2013**, *31* (1), 17–22. https://doi.org/10.1200/JCO.2012.43.1718.

(10) Nastic, D.; Shanwell, E.; Wallin, K.-L.; Valla, M.; Måsbäck, A.; Mateoiu, C.; Lidang, M.; Liakka, A.; Lappi-Blanco, E.; Grove, A.; et al. A Selective Biomarker Panel Increases the Reproducibility and the Accuracy in Endometrial Biopsy Diagnosis. *Int. J. Gynecol. Pathol.* **2017**, *36* (4), 339–347. https://doi.org/10.1097/PGP.0000000000000334.

(11) Ahrens, E. T.; Bulte, J. W. M. Tracking Immune Cells in Vivo Using Magnetic Resonance Imaging. *Nature Reviews Immunology*. October 2013, pp 755–763. https://doi.org/10.1038/nri3531.

(12) Kadayakkara, D. K.; Ranganathan, S.; Young, W. Bin; Ahrens, E. T. Assaying Macrophage Activity in a Murine Model of Inflammatory Bowel Disease Using Fluorine-19 MRI. *Lab. Investig.* **2012**, *92* (4), 636–645.

https://doi.org/10.1038/labinvest.2012.7.

(13) Kennis, B. A.; Michel, K. A.; Brugmann, W. B.; Laureano, A.; Tao, R. H.; Somanchi, S. S.; Einstein, S. A.; Bravo-Alegria, J. B.; Maegawa, S.; Wahba, A.; et al. Monitoring of Intracerebellarly-Administered Natural Killer Cells with Fluorine-19 MRI. *J. Neurooncol.* **2019**, *142* (3), 395–407. https://doi.org/10.1007/s11060-019-03091-5.

(14) Janjic, J. M.; Ahrens, E. T. Fluorine-Containing Nanoemulsions for MRI Cell Tracking. *Wiley Interdiscip. Rev. Nanomedicine Nanobiotechnology* **2009**, *1* (5), 492–501. https://doi.org/10.1002/wnan.35.

(15) Krafft, M. P. Fluorocarbons and Fluorinated Amphiphiles in Drug Delivery and Biomedical Research. *Adv. Drug Deliv. Rev.* **2001**, *47* (2–3), 209–228. https://doi.org/10.1016/S0169-409X(01)00107-7.

(16) Riess, J. G. Understanding the Fundamentals of Perfluorocarbons and Perfluorocarbon Emulsions Relevant to In Vivo Oxygen Delivery. *Artif. Cells, Blood Substitutes, Biotechnol.* **2005**, *33* (1), 47–63. https://doi.org/10.1081/BIO-200046659.

(17) Partlow, K. C.; Chen, J.; Brant, J. A.; Neubauer, A. M.; Meyerrose, T. E.; Creer, M. H.; Nolta, J. A.; Caruthers, S. D.; Lanza, G. M.; Wicldine, S. A. 19F Magnetic Resonance Imaging for Stem/Progenitor Cell Tracking with Multiple Unique Perfluorocarbon Nanobeacons. *FASEB J.* **2007**, *21* (8), 1647–1654. https://doi.org/https://doi.org/10.1096/fj.06-6505com.

(18) Maa, Y.-F.; Hsu, C. C. Performance of Sonication and Microfluidization for Liquid–Liquid Emulsification. *Pharm. Dev. Technol.* **1999**, *4* (2), 233–240.

https://doi.org/10.1081/PDT-100101357.

(19) Varescon, Christian; Arlen, Christian; Le Blanc, Maurice; G. Riess, Jean. An Easy, Convenient Way of Describing the Stability of Fluorocarbon Emulsions. *J. Chim. Phys.* **1989**, *86*, 2111–2117. https://doi.org/10.1051/jcp/1989862111.

(20) Hingorani, D. V.; Chapelin, F.; Stares, E.; Adams, S. R.; Okada, H.; Ahrens, E. T. Cell Penetrating Peptide Functionalized Perfluorocarbon Nanoemulsions for Targeted Cell Labeling and Enhanced Fluorine-19 MRI Detection. *Magn. Reson. Med.* **2020**, *83* (3), 974–987. https://doi.org/10.1002/mrm.27988.

(21) Janjic, J. M.; Srinivas, M.; Kadayakkara, D. K. K.; Ahrens, E. T. Self-Delivering Nanoemulsions for Dual Fluorine-19 MRI and Fluorescence Detection. *J. Am. Chem. Soc.* **2008**, *130* (9), 2832–2841. https://doi.org/10.1021/ja077388j.

(22) Li, S.; Wang, L.; Li, N.; Liu, Y.; Su, H. Combination Lung Cancer Chemotherapy: Design of a PH-Sensitive Transferrin-PEG-Hz-Lipid Conjugate for the Co-Delivery of Docetaxel and Baicalin. *Biomed. Pharmacother.* **2017**, *95* (27), 548–555. https://doi.org/10.1016/j.biopha.2017.08.090.

(23) Srinivas, M.; Morel, P. A.; Ernst, L. A.; Laidlaw, D. H.; Ahrens, E. T. Fluorine-19 MRI for Visualization and Quantification of Cell Migration in a Diabetes Model. *Magn. Reson. Med.* **2007**, *58* (4), 725–734. https://doi.org/10.1002/mrm.21352.

(24) Butler, P. J.; Harris, J. I.; Hartley, B. S.; Lebeman, R. The Use of Maleic Anhydride for the Reversible Blocking of Amino Groups in Polypeptide Chains. *Biochem. J.* **1969**, *112* (5), 679–689. https://doi.org/10.1042/bj1120679.

(25) Ning, X.; Guo, J.; Wolfert, M. A.; Boons, G.-J. Visualizing Metabolically-Labeled Glycoconjugates of Living Cells by Copper-Free and Fast Huisgen Cycloadditions

**. https://doi.org/10.1002/anie.200705456.

(26) Krämer, W.; Grapentin, C.; Bouvain, P.; Temme, S.; Flögel, U.; Schubert, R. Rational Manufacturing of Functionalized, Long-Term Stable Perfluorocarbon-Nanoemulsions for Site-Specific 19F Magnetic Resonance Imaging. *Eur. J. Pharm. Biopharm.* **2019**, *142* (June), 114–122. https://doi.org/10.1016/j.ejpb.2019.06.014.

(27) Liu, F.; Liang, Y.; Houk, K. N. Bioorthogonal Cycloadditions: Computational Analysis with the Distortion/Interaction Model and Predictions of Reactivities. *Acc. Chem. Res.* **2017**, *50* (9), 2297–2308. https://doi.org/10.1021/acs.accounts.7b00265.

(28) Mushtaq, S.; Yun, S. J.; Jeon, J. Recent Advances in Bioorthogonal Click Chemistry for Efficient Synthesis of Radiotracers and Radiopharmaceuticals. *Molecules*. MDPI AG October 2, 2019. https://doi.org/10.3390/molecules24193567.

(29) Lee, S. B.; Kim, H. L.; Jeong, H.-J.; Lim, S. T.; Sohn, M.-H.; Kim, D. W. Mesoporous Silica Nanoparticle Pretargeting for PET Imaging Based on a Rapid Bioorthogonal Reaction in a Living Body. *Angew. Chemie* **2013**, *125* (40), 10743–10746. https://doi.org/10.1002/ange.201304026.

(30) Jewett, J. C.; Sletten, E. M.; Bertozzi, C. R. Rapid Cu-Free Click Chemistry with Readily Synthesized Biarylazacyclooctynones. *J. Am. Chem. Soc.* **2010**, *132* (11), 3688–3690. https://doi.org/10.1021/ja100014q.

(31) Laughlin, S. T.; Baskin, J. M.; Amacher, S. L.; Bertozzi, C. R. In Vivo Imaging of Membrane-Associated Glycans in Developing Zebrafish. *Science (80-.).* **2008**,

320 (5876), 664–667. https://doi.org/10.1126/science.1155106.

(32) Devaraj, N. K.; Upadhyay, R.; Haun, J. B.; Hilderbrand, S. A.; Weissleder, R. Fast and Sensitive Pretargeted Labeling of Cancer Cells through a Tetrazine/Trans-Cyclooctene Cycloaddition. *Angew. Chemie - Int. Ed.* **2009**, *48* (38), 7013–7016. https://doi.org/10.1002/anie.200903233.

(33) Dommerholt, J.; Rutjes, F. P. J. T.; Van Delft, F. L.; Vrabel, M.; Carell, T.; Nl, F. V. Strain-Promoted 1,3-Dipolar Cycloaddition of Cycloalkynes and Organic Azides. *Top. Curr. Chem. 374*. https://doi.org/10.1007/s41061-016-0016-4.

(34) Ahrens, E. T.; Flores, R.; Xu, H.; Morel, P. A. In Vivo Imaging Platform for Tracking Immunotherapeutic Cells. *Nat. Biotechnol.* **2005**, *23* (8), 983–987. https://doi.org/10.1038/nbt1121.

(35) Ben, J.; Zhu, X.; Zhang, H.; Chen, Q. Class A1 Scavenger Receptors in Cardiovascular Diseases. *Br. J. Pharmacol.* **2015**, *172* (23), 5523–5530. https://doi.org/10.1111/bph.13105.

(36) Tang, T.; Valenzuela, A.; Petit, F.; Chow, S.; Leung, K.; Gorin, F.; Louie, A. Y.; Dhenain, M. In Vivo MRI of Functionalized Iron Oxide Nanoparticles for Brain Inflammation. *Contrast Media Mol. Imaging* **2018**, *2018*. https://doi.org/10.1155/2018/3476476.

(37) Jahromi, A. H.; Wang, C.; Adams, S. R.; Zhu, W.; Narsinh, K.; Xu, H.; Gray, D. L.; Tsien, R. Y.; Ahrens, E. T. Fluorous-Soluble Metal Chelate for Sensitive Fluorine-19 Magnetic Resonance Imaging Nanoemulsion Probes. *ACS Nano* **2019**, *13* (1), 143–151. https://doi.org/10.1021/acsnano.8b04881.

(38) Flores, A.; Ize, P.; Ramos, S.; Castillo, R. The Dioctadecylamine Monolayer:

Textures, Phase Transitions, and Dendritic Growth. *J. Chem. Phys.* **2003**, *119* (11), 5644–5653. https://doi.org/10.1063/1.1598951.

(39) Helmer, K. G.; Han, S.; Sotak, C. H. On the Correlation between the Water Diffusion Coefficient and Oxygen Tension in RIF-1 Tumors. *NMR Biomed.* **1998**, *11* (3), 120–130. https://doi.org/10.1002/(sici)1099-1492(199805)11:3<120::aid-nbm506>3.0.co;2-%23.

(40) Dardzinski, B. J.; Sotak, C. H. Rapid Tissue Oxygen Tension Mapping Using19F Inversion-Recovery Echo-Planar Imaging of P Erfluoro-15 -Crown-5-Ether. *Magn. Reson. Med.* **1994**, *32* (1), 88–97. https://doi.org/10.1002/mrm.1910320112.

(41) Mizukami, S.; Takikawa, R.; Sugihara, F.; Hori, Y.; Tochio, H.; Wälchli, M.; Shirakawa, M.; Kikuchi, K. Paramagnetic Relaxation-Based 19F MRI Probe to Detect Protease Activity. *J. Am. Chem. Soc.* **2008**, *130* (3), 794–795. https://doi.org/10.1021/ja077058z.

(42) Gonzales, C.; Yoshihara, H. A. I.; Dilek, N.; Leignadier, J.; Irving, M.; Mieville, P.; Helm, L.; Michielin, O.; Schwitter, J. In-Vivo Detection and Tracking of T Cells in Various Organs in a Melanoma Tumor Model by 19F-Fluorine MRS/MRI. *PLoS ONE*. 2016. https://doi.org/10.1371/journal.pone.0164557.

(43) Greg T. Hermanson. *Bioconjugate Techniques*, 2nd ed.; Pierce Biotecnology, Ed.; Thermo Fischer Scientific, 2008.

(44) Pickens, C. J.; Johnson, S. N.; Pressnall, M. M.; Leon, M. A.; Berkland, C. J. Practical Considerations, Challenges, and Limitations of Bioconjugation via Azide-Alkyne Cycloaddition. *Bioconjug. Chem.* **2018**, *29* (3), 686–701. https://doi.org/10.1021/acs.bioconjchem.7b00633.

(45) Kim, S.; Ko, W.; Sung, B. H.; Kim, S. C.; Lee, H. S. Direct Protein–Protein Conjugation by Genetically Introducing Bioorthogonal Functional Groups into Proteins. *Bioorganic Med. Chem.* **2016**, *24* (22), 5816–5822. https://doi.org/10.1016/j.bmc.2016.09.035.